Discrete-Time Adaptive PID Current Controller for Wind Boost Converter

David R. López-Flores, *Student Member, IEEE*, José L. Durán-Gómez, *Senior Member, IEEE,* and Javier Vega-Pineda, *Member, IEEE*

***Abstract*—This paper proposes an adaptive controller for a dc-dc boost converter to regulate the output current levels of a 400 W small wind turbine based on a permanent magnet synchronous generator with a three-phase diode rectifier. Despite the stochastic nature of wind, this discrete-time adaptive PID controller regulates the current levels without large overshoots and oscillations to attain the maximum power point of the wind system. The adaptive mechanism algorithm operating with two electrical measurements adjusts the controller parameters, and is designed with an approach consisting of the integration of the variable operation point of the small wind turbine into the discrete-time model of the dc-dc boost converter and the Bode stability criteria. The mechanism algorithm features a low computational complexity for controller parameters estimation and therefor a practical implementation in a low-end micro-controller (small size, low cost, and low energy consumption) is possible. Furthermore, the results based on the processor-in-the-loop simulation approach show that controlling the current levels and the maximum power point of the wind system via the proposed adaptive controller is more effective than a controller tuned around a particular fixed operating point.**

***Index Terms*—Discrete-time, adaptive control, DC-DC boost converter, wind energy conversion system, processor-in-the-loop simulation.**

I. Introduction

The development of wind energy conversion systems (WECS) has made a viable alternative in wind energy harvesting to climate change mitigation [1], [2]. Because of its easy handling and low cost, a small wind turbine (SWT) based on a permanent magnet synchronous generator (PMSG) is widely used in small-scale wind turbine systems. Taking into account the nature of stochastic wind, the SWT generates a wide range of voltage and current at its output terminals which need to be controlled at certain levels without large overshoots and oscillations to attain its maximum power point (MPP) effectively. These output levels, which correspond to an optimal voltage or current trajectory determined by the maximum power point tracking algorithm, are typically tracked by a dc-dc boost converter with the appropriate control scheme and controllers [3]–[8]. In this regard, the proportional-integral (PI) controller tuned around a particular fixed operating point of the wind system along with a cascade or single control scheme has been the preferred controller by the scientific community [9]–[13].

The stochastic nature of wind leads to a wind system's variable operation point and large fluctuations around the optimal trajectory of voltage or current. The fluctuating operation point presents a challenge for the PI controller performance, because must track the optimal trajectory with minimal oscillations and overshoots, M_p, to guarantee the wind system stability along the tracking process of the maximum power point (MPPT). Furthermore, less severe electrical and mechanical problems in the wind system, such as stressed electromechanical and saturated power systems must be secured. According to [14] and the Bode stability criterion [15], the oscillations and overshoots, M_p, are minimized when a controller allows maintaining both a phase (PM) and gain margin (GM) of at least 30º and 10 dB, respectively. However, to ensure these PM and GM margins in a renewable energy or wind system operates with a variable operating point and a fluctuating optimal trajectory it requires a suitable adaptive mechanism algorithm that adjusts the controller parameters. The adaptive proportional–integral–derivative (PID) controller proposed in [16] is very close in this regard. The authors presented a back-propagation training approach combined with a neuro-fuzzy multiple-input multiple-output (MIMO) system and reference model was used in the adaptive algorithm to adjust the parameters of the adaptive PID controller, which tracks an optimal voltage trajectory using a voltage control scheme. The adaptive algorithm in [17], used a multiple-input single-output (MISO) fuzzy system to adjust the parameters of an adaptive PI controller for tracking an optimal voltage trajectory using a cascade control scheme comprised of an inner current loop and an outer voltage loop. This controller was used in the outer voltage loop to provide the reference current in the cascade control scheme. The work in [18] used a similar control scheme to [17], consisting on a non-linear current control approach and adaptive voltage controller in the inner and outer loop, respectively. The parameters of this adaptive controller were adjusted via an adaptive algorithm that has an observer, which decomposes the electrical measurements of voltage and current in the dq reference frame. An adaptive sliding mode controller with a PI sliding surface was described in [19]. This controller used an observer to estimate variables of the renewable source, such as voltages and currents. These variables were used in the adaptive controller to properly adjust the control signal dc-dc converter of the renewable source. Finally, the work of [20] used an adaptive controller in the voltage control scheme. The parameters of this controller were adjusted by an adaptive algorithm designed via the MIT (Massachusetts Institute of Technology) rule approach, which combines the gradient method with a reference model to track the optimal voltage trajectory effectively.

The above approaches lead to suitable adaptive mechanism algorithms for estimating the parameter adjustments of the adaptive controllers and effectively tracking the optimal trajectory of the renewable source without large oscillations

David R. López-Flores, José L. Durán-Gómez, and Javier Vega-Pineda are with Tecnológico Nacional de México / IT de Chihuahua, Ave. Tecnológico 2909 Chihuahua, México, emails: D17061537@chihuahua.tecnm.mx, jose.dg@chihuahua.tecnm.mx, and javier.vp01@chihuahua.tecnm.mx.

and overshoots, M_p. However, according to the computational complexity theory [21], the complex nature of the neuro-fuzzy systems and the MIMO/MISO fuzzy systems lead to adaptive algorithms with an estimation complexity greater than a constant complexity, $O(1)$; the greater complexity is due to the number of neurons and rules used in the neural and fuzzy systems. The execution time of an algorithm is negatively affected by the increment in its complexity estimation or by using observers based on variable estimation methods; this difficulting the implementation of an adaptive controller in low-end microcontrollers (small size, low cost, and low energy consumption). Besides, a challenge in adaptive algorithms that use reference models, is that they must adequately represent the system dynamics under control to adjust the controller parameters. To overcome this challenge, it is convenient to obtain the reference model through open-loop experimental tests without any control scheme. Unfortunately, there are systems whose nature makes this testing difficult and risky. Also, the control schemes based on a single voltage loop can lead to large peak currents in the renewable system along the MPPT process. These large peak currents are mainly due to the absence of a current control loop. Additionally, the stochastic nature of wind can lead to unwanted dynamic interactions between the inner and outer loop of the cascade control scheme and may result in a MPPT process adversely affected. Finally, the effectiveness of these adaptive algorithms was not demonstrated against a profile of the renewable source with low- and high-frequency power components and random noise (RN) conditions.

This paper presents a current control scheme that uses a discrete-time adaptive PID controller with a first-order derivative filter to effectively attain the MPP of a 400 W wind system comprised of a small-scale wind turbine connected to a battery bank via a PMSG generator along whit a front-end three-phase diode rectifier coupled to a dc-dc boost converter. The parameters of this controller are adjusted via an adaptive mechanism algorithm designed with an approach consisting of the integration of the variable operation point of the small wind turbine into the discrete-time model of the dc-dc boost converter and the Bode stability criteria. This approach leads to the following contributions:

i. Effective control of the output current levels and the MPP of the wind system, as well as of the tracking of the optimal current trajectory without larger oscillations and overshoots, M_p. This is demonstrated via the processor-in-the-loop (PIL) simulation approach when the wind system is subjected to a wind profile with low- and high-frequency power components along with random noise conditions.
ii. The parameters of the adaptive controller are adjusted based on two electrical measurements without reference models or observers.
iii. The adaptive controller can be implemented in low-end microcontrollers due to the parameter adjustment adaptive algorithm's low estimation complexity, $O(1)$.
iv. The low number of electrical measurements and estimation complexity leads to a low-cost and practical implementation of the adaptive controller in small-scale wind turbine systems.

This paper is organized as follows. First, a detailed description of the wind system and the adaptive mechanism algorithm used in the proposed adaptive controller are introduced in Section II. Then, the circuit implementation of the wind system and the adaptive controller based on PIL simulation approach are presented in Section III. Section IV presents the PIL simulation results and discussions aimed to demonstrate the performance and effectiveness of the proposed adaptive controller when the wind system is subjected to a wind profile with low- and high-frequency power components and RN conditions. Finally, the conclusions are given in Section V.

II. Adaptive Controller for The Wind System

This section presents the description of the small-scale wind turbine system and the methodology used to design the proposed adaptive controller.

A. System Description

The block diagram of the small-scale wind turbine system is shown in Fig. 1. It comprises of eight parts: the wind turbine, the electric generator, the rectifier, the MPPT algorithm, the proposed adaptive controller, the dc-dc power converter, the battery bank and the filters.

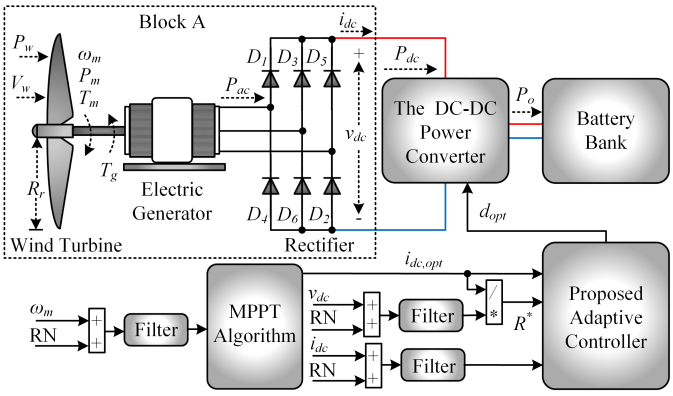

Fig. 1. Block diagram of the small-scale wind turbine system.

The parts of the small-scale wind turbine system depicted in Fig. 1 are described next.

1) *Wind Turbine*. Consists of a horizontal axis SWT with three blades of radius R_r = 0.575 m. This SWT converts the wind power, P_w [w], to mechanical power, P_m [w], through its blades and rotor. The static and dynamic model of the SWT is developed based on [22] and [23], respectively. In the SWT model, the mechanical and electrical parameters were considered from a small-scale wind power electricity generation training system of a FESTO wind turbine learning model [24]. According to Fig. 1, the variables V_w [m/s], ω_m [rad/s], T_m [N·m], and T_g [N·m] represent the wind speed, the rotational speed, the mechanical torque, and the electrical torque, respectively.
2) *Electric Generator*. This part corresponds to the PMSG generator, and its model is developed via the dq-synchronous rotating reference frame from [25]. The

PMSG converts the mechanical power, P_m, from the SWT into the AC electrical power, P_{ac} [w].

3) *Rectifier*. It consists of a front-end three-phase diode rectifier (PDT), which converts the AC electrical power, P_{ac}, into dc electrical power, P_{dc} [w]. The PDT model is taken from the simulator electrical block libraries.
4) *MPPT Algorithm*. This part consists of an algorithm based on the power signal feedback (PSF) technique [26]. Using the rotational speed, ω_m, single measurement, this algorithm estimates the optimal current trajectory, $i_{dc,opt}$, for the proposed adaptive controller. According to Fig. 1, the variable R^* represents the variable operation point of the small wind turbine at its MPP, and it is estimated by dividing the rectifier output voltage, v_{dc}, by the optimal current trajectory, $i_{dc,opt}$.
5) *Proposed Adaptive Controller*. It consists of a discrete-time adaptive PID controller with a first-order derivative filter. Based on the optimal current trajectory , $i_{dc,opt}$, the variable operation point , R^*, and the measured value of the rectifier output current, i_{dc}, this controller estimates the optimal duty cycle signal, d_{opt}, to attain a suitable adjustment in the dc-dc power converter impedance. The adaptive controller design and its circuit implementation in a simulator are presented in detail in Sections II.B and III.A, respectively.
6) *The DC-DC Power Converter*. This part corresponds to the boost circuit topology in which its impedance adjusted via the optimal duty cycle signal , d_{opt}, allows to control the rectifier output voltage and current at certain levels to attain the MPP of the small wind turbine.
7) *Battery Bank*. This block to store the energy is formed by a series arrangement of lithium-ion (Li-on) batteries with a nominal voltage, V_{nom}, of 200 V, which comes from the dc-dc boost converter. Its mathematical model is taken from [27].
8) *Filters*. They consist of Kalman filters employed to remove the RN mounted on the electrical signals of the rectifier output voltage , v_{dc}, and current, i_{dc}, as well as the the rotational speed , ω_m, measurement. The main idea of implementing the filters in the wind system is to assess the performance of the adaptive controller under the RN situations. The Kalman filter models are designed based on [28].

B. Proposed Adaptive Controller

According to [22], the accurate aerodynamic efficiency of the SWT is determined by a non-linear polynomial function which is called the power coefficient, C_p. This function tells how efficiently a wind turbine converts the wind power, P_w, to mechanical power, P_m. Differently to [22], this function was designed based on the experimental data set of the FESTO wind turbine learning system via a curve-fitting approach, as defined by (1):

$$C_p = c_1\lambda^7 + c_2\lambda^6 + c_3\lambda^5 + c_4\lambda^4 + c_5\lambda^3 + c_6\lambda^2 + c_7\lambda + c_8 \quad (1)$$

where c_i are constant values and the λ variable represents the ratio between the tangential speed of the tip of a wind turbine blade and the wind speed, V_w, as follows:

$$\lambda = \frac{\omega_m R_r}{V_w} \quad (2)$$

According to [29] and [30], as well as the power coefficient , C_p, the conversion of wind power to mechanical power is determined as follows:

$$P_m = C_p(\lambda)P_w = \frac{1}{2}C_p(\lambda)\rho\pi R_r^2 V_w^3 \quad (3)$$

where ρ is the air density. The behavior of the power coefficient, C_p, shown in Fig. 2, is produced by considering the simulation parameters in Tables I - II from the appendix, a wind speed, V_w, of 10 m/s in Block A of Fig. 1 with a resistive sweep load, $R_{sweep,load}$, performed at the rectifier output.

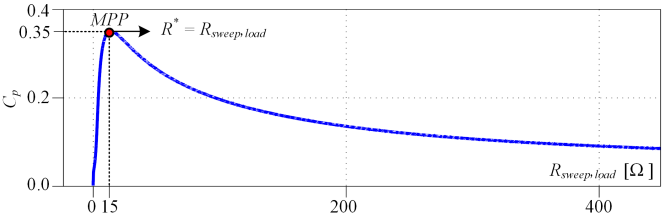

Fig. 2. Curve of C_p versus $R_{sweep,load}$ for a V_w = 10 m/s.

The maximum value of the power coefficient, C_p, is reached when the resistive sweep load, $R_{sweep,load}$, is close to 15 Ω. Under this condition, the R^* value is considered as the operation point of the SWT and corresponds to its MPP. This behavior is repeated for a wide range of wind speed operations; hence the value of the operation point of the SWT, R^*, is variable. Since this operation point is estimated by dividing the rectifier output voltage, v_{dc}, by the optimal current trajectory, $i_{dc,opt}$, the Block A in Fig. 1 can be replaced by the variable operation point, R^*, and integrated into the dc-dc boost converter electronic diagram, as shown in Fig. 3.

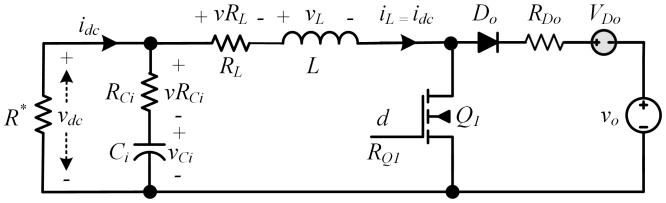

Fig. 3. Integration of the variable operation point, R^*, into the dc-dc boost converter electronic diagram.

From Fig. 3, C_i, R_{Ci}, v_{Ci}, and vR_{Ci} represents the input capacitor, the internal resistance of the capacitor, the voltage drop of the capacitor, and the voltage drop of the capacitor internal resistance, respectively. L, i_L, R_L, v_L, and v_{RL} represents the inductor, the inductor current, the internal resistance of the inductor, the voltage drop of the inductor, and the voltage drop of the inductor internal resistance, respectively. Transistor Q_1 is the actuator that adjusts the impedance of the dc-dc boost converter based on the modulated d signal. The internal resistance of Q_1 is represented by R_{Q1}. The output diode, D_o, is represented by a forward voltage drop, V_{Do}, and an internal resistance, R_{Do}. The connection between the battery bank and the dc-dc boost converter is passive. This type of connection and the slow dynamics of the battery bank lead to considering the output voltage, v_o, as a constant parameter [31]. Applying the state-space averaging technique of [14] in

the electronic diagram of Fig. 3, the mathematical model of the dc-dc Boost converter along with the variable operation point is obtained as follow:

$$\frac{di_L}{dt} = -\left(\frac{R_{Do}+R_L+R_{Do}d}{L}\right)i_L + \frac{v_{dc}}{L} + \left(\frac{d-1}{L}\right)V_{Do} + \left(\frac{d-1}{L}\right)v_o \tag{4}$$

$$\frac{dv_{dc}}{dt} = \left(\frac{R_{Do}R_{C_i}R^* + R_LR_{C_i}R^* - R_{Do}R_{C_i}R^*d}{LR_{C_i}+LR^*}\right)i_L + \left(\frac{R_{Q1}R_{C_i}R^*d}{LR_{C_i}+LR^*}\right)i_L - \left(\frac{R^*}{C_iR_{C_i}+C_iR^*}\right)i_L + \left(\frac{1}{C_iR_{C_i}+C_iR^*} - \frac{R_{C_i}R^*}{LR_{C_i}+LR^*}\right)v_{dc} + \left(\frac{R_{C_i}R^* - {R_{C_i}}^2d}{LR_{C_i}+LR^*}\right)V_{Do} + \left(\frac{R_{C_i}R^* - {R_{C_i}}^2d}{LR_{C_i}+LR^*}\right)v_o \tag{5}$$

Considering a current control scheme and that the effects of the inductor internal resistance, R_L, the diode internal resistance, R_{DO}, the diode forward voltage drop, V_{Do}, and the transistor internal resistance, R_{Q1}, are neglected in (4) and (5). Then, the open-loop transfer function of the system between the inductor current, i_L, and the duty cycle signal, d, is defined by:

$$G_{i_Ld}(s) = \frac{(C_iR_{C_i}V_o + C_iR^*V_o)s + V_o}{(C_iLR_{C_i}+C_iLR^*)s^2 + (L+C_iR_{C_i}R^*)s + R^*} \tag{6}$$

Based on the theory developed in [32], the internal resistance of the input capacitor, R_{C_i}, varies with its operating frequency and temperature. Hence, it is essential to evaluate the effect of this resistance over the open-loop response of the system (6). According to the above, the input capacitor, C_i, the inductor, L, the switching frequency, f_s, and the operation point, R^*, are 470 μf, 80 mH, 5 kHz, and 15 Ω, respectively. Then, in Fig. 4 (a) and (b) are shown the effects of this internal resistance, R_{C_i}, on the open-loop step response as well as in the Bode diagram of system (6), respectively. It is easy to notice in Fig. 4 that variations of the internal resistance of the capacitor, R_{C_i}, do not cause significant changes in the GM and PM as shown in the Bode diagram of Fig. 4 (b), which leads to small changes of the value of the overshoot, M_p, in the open-loop step response of Fig. 4 (a). Therefore, the system (6) can be simplified as:

$$G_{i_Ld}(s) = \frac{C_iR^*V_os + V_o}{C_iLR^*s^2 + Ls + R^*} \tag{7}$$

The input signal to the system (7) is the duty cycle signal, d, which is generated via the digital pulse width modulation technique (DPWM). The transfer function of this DPWM is based on its number of bits, b, as follows:

$$K_{DPWM}(s) = \frac{1}{2^b - 1} \tag{8}$$

Considering in this work a discrete-time adaptive PID current controller in Fig. 1, the DPWM synchronizes the process of the feedback signal acquisition represented by the inductor current, i_L, and updates the duty cycle signal, d, as it is shown in Fig. 5.

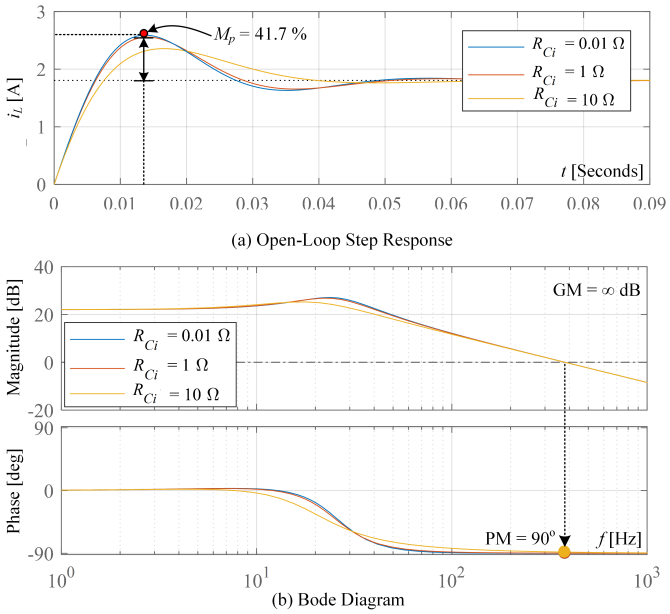

Fig. 4. The R_{C_i} effects on the open-loop step response as well as on the Bode diagram of the system (6).

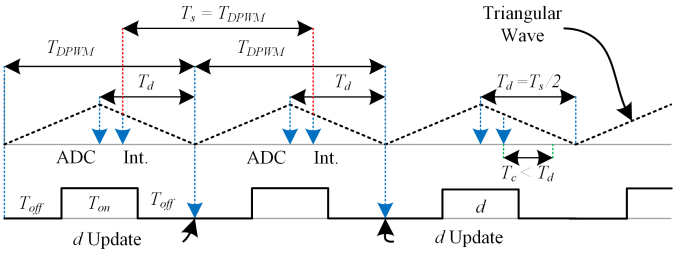

Fig. 5. Synchronization process for the feedback signal acquisition, i_L, and updating the d signal via the DPWM.

A digital triangular wave signal with same period than the digital modulator, T_{DPWM}, keeps the synchronization process. In the middle of the T_{DPWM} period, an analog-to-digital converter (ADC) begins the process of acquiring the inductor current, i_L, signal and converting it into a digital signal. Finishing this process, the ADC generates interrupt signal, Int., which is used to activate the code section corresponding to the adaptive digital controller. The computation time, T_c, of this controller must be inferior to the time delay, T_d, to guarantee stability in the system (7). The sampling period (T_s), which is equivalent to the T_{DPWM} period, is the time difference between the ADC interruptions. The time delay, T_d, is between the ADC starting a conversion process and the duty cycle signal, d, update; therefore, $T_d = T_s/2$. T_d leads to a delay on the system (7), and its transfer function is given by:

$$G_{T_D}(s) = e^{-sT_d} \tag{9}$$

Then, according to the synchronization process shown in Fig. 5, the appropriate method for the system (7) discretization is the zero-order hold (ZOH) [15]:

$$G_{i_Ld}(z) = Z\left[(8)(9)\frac{1-e^{-sT_s}}{s}\frac{C_iR^*V_os + V_o}{C_iLR^*s^2 + Ls + R^*}\right] \tag{10}$$

Resulting in the following symbolic expression:

$$G_{i_L d}(z) = K_G \frac{(z + z_{1,G})(z + z_{2,G})}{z(z - e^{-aT_s})(z - e^{-bT_s})} \tag{11}$$

where the parameters K_G, $[z_{1,G},\ z_{2,G}]$, and $[e^{-aT_s},\ e^{-bT_s}]$ represent the gain, zeros, and poles of the system (11), respectively. These parameters are computed considering the diode internal resistance, R_{DO}, and the diode forward voltage drop, V_{Do}, of 42 mΩ and 0.7 V, respectively, and the variable operation point, R^*.

The open-loop step response normalized to unity and the Bode diagram of the discrete system (11) considering the different values of wind speed, V_w, are shown in Fig. 6 (a) and (b), respectively.

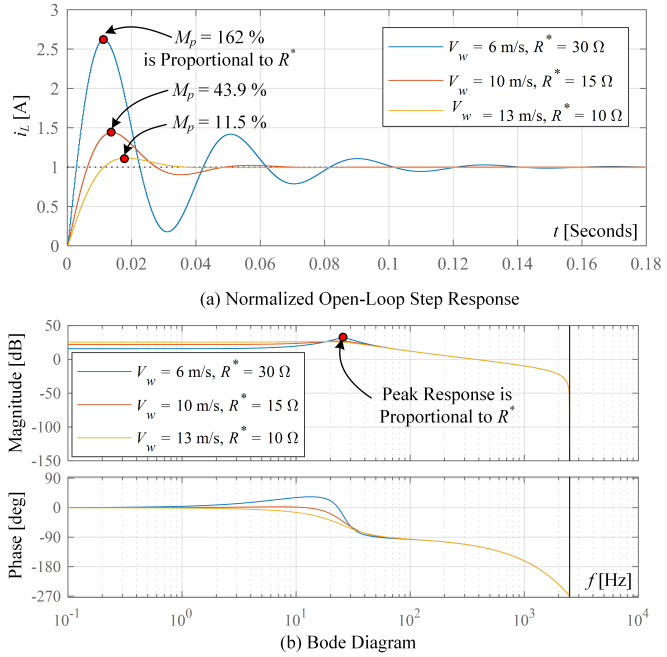

(a) Normalized Open-Loop Step Response

(b) Bode Diagram

Fig. 6. Normalized open-loop step response and the Bode diagram of the discrete system (11), applying different V_w values.

Figs. 6 (a) and (b) show that an increase of the operation point, R^*, which is inversely proportional to the value of the wind speed, V_w, leads to large overshoots, M_p, and oscillations as well as an increase in the peak response, respectively. Therefore, the digital current control scheme depicted in Fig. 1 must adapt its parameters via a suitable adaptive mechanism algorithm to guarantee acceptable GM and PM values which allow minimize the overshoots, M_p, and oscillations of the inductor current, i_L, along the tracking process of the optimal current trajectory, $i_{dc,opt}$, to attain the MPP of the wind system effectively. The adaptive algorithm is described next.

The discrete-time adaptive PID controller with a first-order derivative filter used as the digital current control scheme is modeled as follows:

$$C(z) = \frac{d_{opt}(z)}{i_{dc,opt} - i_{dc}(z)} = K_C \frac{(z - z_{1,C})(z - z_{2,C})}{(z - p_{1,C})(z - p_{2,C})} \tag{12}$$

where the parameters K_C, $[z_{1,C},\ z_{2,C}]$, and $[p_{1,C},\ p_{2,C}]$ represent the gain, zeros, and poles of the the digital controller, respectively. Considering the Bode stability criterion and the variable operation point, R^*, the online computation criteria to adjust the parameters can be proposed via a system gain, poles and zeros cancellation approach (11) to attain acceptable PM and GM margins along the MPPT process. These online computation criteria are presented below:

- The digital controller gain, K_C, is programmed to cancel out the system (11) gain, K_G, in order to obtain an acceptable closed-loop rise time response.
- To minimize a phase drop due to the two poles of the system (11), $[e^{-aT_s},\ e^{-bT_s}]$, the zeros, $[z_{1,C},\ z_{2,C}]$, of the digital controller are used to cancel these poles, respectively.
- The first pole of the digital controller, $p_{1,C}$, is used as an integrative action and positioned at 0 Hz, while second pole, $p_{2,C}$, is used to cancel the second zero of the system (11), $z_{2,G}$. This criterion minimizes the variations of the PM and GM margins versus the different values of the operation point, R^*.

According to the previous criteria and the current control scheme depicted in Fig. 1, then Fig. 7 shows the adaptive mechanism algorithm block diagram that dynamically adjusts the parameters of (12).

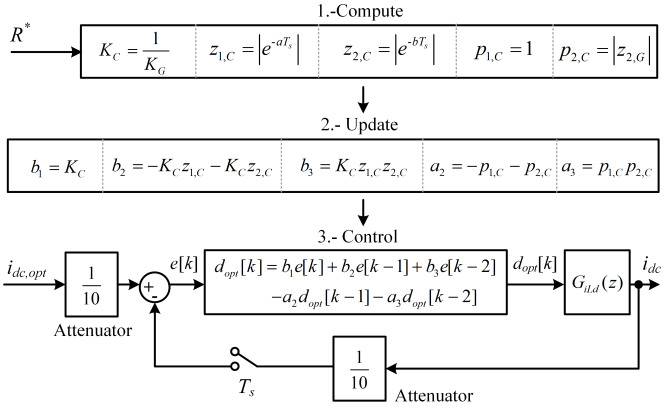

Fig. 7. Block diagram of the proposed adaptive mechanism algorithm to adjust the discrete-time adaptive PID control interface parameters.

The adaptive mechanism algorithm depicted in Fig. 7 comprises three steps:

1) *Compute*. The K_C, $z_{1,C}$, $z_{2,C}$, $p_{1,C}$, and $p_{2,C}$ parameters are estimated as depicted in Fig. 7 using the online computation criteria and the value of the variable operation point, R^*.
2) *Update*. The a_i and b_i coefficients are updated based on the K_C, $z_{1,C}$, $z_{2,C}$, $p_{1,C}$, and $p_{2,C}$ parameters using the equations depicted in Fig. 7, which are previously obtained by the next two steps. The first step consists of applying the difference equation method of [15] in (12), resulting in expression (13) to appropriately compute the optimal duty cycle signal, d_{opt}. In the second step, the coefficient equating method is used between (12) and (13) to determine the a_i and b_i equations.

$$\begin{aligned} d_{opt}[k] = {} & b_1 e[k] + b_2 e[k-1] + b_3 e[k-2] \\ & - a_2 d_{opt}[k-1] - a_3 d_{opt}[k-2] \end{aligned} \tag{13}$$

3) *Control*. Using the a_i and b_i coefficients, the controller (12) represented by the difference equation (13) processes

the error signal, e_k, based on the difference between the values of the optimal current trajectory, $i_{dc,opt}$, and the rectifier output currrent, i_{dc}. As a result, the optimal duty cycle signal, d_{opt}, is obtained to properly adjust the dc-dc boost converter input impedance. This adjustment leads to a suitable control of the rectifier output current without large overshoots, M_p, and oscillations. Consequently, the MPP of the small-scale wind turbine system is effectively attained.

It can be deduced from Fig. 7 that the digital current controller parameters are estimated using the electrical measurements of the rectifier output voltage, v_{dc}, and the rectifier output currrent, i_{dc}, without reference models or observers. In addition, the required computations to carry out this estimation are based on multiplication, addition, subtraction, exponential function, and division. According to the computational complexity theory developed in [21], an algorithm designed through this type of operations derived from the proposed adaptive mechanism leads to an algorithm with a constant estimation complexity, $O(1)$. Therefore, based on these deductions, the proposed adaptive controller shown in Fig. 7 results in a low-cost and practical implementation in small-scale wind turbine systems as well as a practical implementation in low-end microcontrollers.

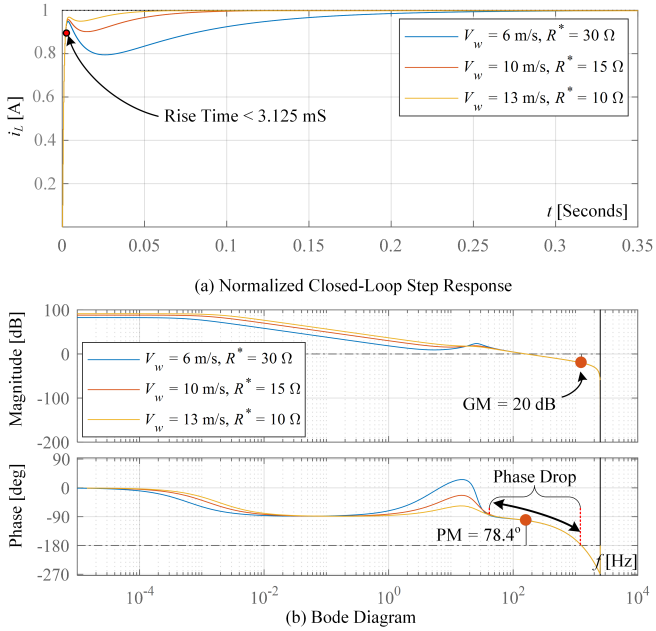

Fig. 8. Normalized closed-loop step response and the Bode diagram of the discrete system (11) via the proposed adaptive controller versus different V_w values.

Considering different values of wind speed, V_w, Figs. 8 (a) and (b) show the closed-loop step response normalized to unity and Bode diagram, respectively, of the system (11) operating with the current control scheme depicted in Fig. 7 to demonstrate the performance of the proposed adaptive controller. Fig. 8 (b) also shows that the GM and PM margins remain within the ranges and minimal variations; as a result, the overshoots, M_p in the inductor current, i_L, are minimized, and the closed-loop rise time response is acceptable, see Fig. 8 (a). In addition, the computation criteria to adjust the parameters in the proposed adaptive controller, allows to smooth the phase drop that is close to the value of 78.4^o, see Fig. 8 (b). As a result of this, stability and robustness are guaranteed against possible PM margin displacements caused by the changes of the wind speed, V_w, and external situations, such as the dynamics of both the Kalman filters and the SWT.

Replacing the PID current controller in Fig. 7 with a PI controller tuned around the particular operating point of wind speed, V_w, of $10m/s$, then, Figs. 9 (a) and (b) show the closed-loop step response normalized to unity and the Bode diagrams, respectively, of the system (11) versus different values of wind speed, V_w. It can be seen in Fig. 9 (b) that the tuned PI controller leads to essential changes in the margins of GM and PM, as a result of this; large values of overshoots, M_p and oscillations are presented in the inductor current, i_L, as well as an increase in the closed-loop rise time response, see Fig. 9 (a). Additionally, unlike the phase drop depicted in Fig. 8 (b), the phase drop shown in Fig. 9 (b) is more pronounced; this leads to a higher sensitivity in the changes of the overshoots, M_p, and oscillations of the inductor current, i_L, versus different values of wind speed, V_w, as well as external situations. Hence, an adaptive controller with an appropiate adaptive mechanism algorithm is more convenient than one tuned around a particular fixed operating point to ensure robustness and stability in the small-scale wind turbine system.

III. Simulation Results and Discussions

In order to demonstrate the proposed adaptive controller performance, this section describes the entire simulation circuit implementation of the small-scale wind turbine system and the simulation results with their discussions considering the parameters in Tables I and II shown in the appendix.

A. Simulation Circuit Implementation

Based on the PIL simulation approach used in [33], the simulation circuit implementation of the small-scale wind turbine system is shown in Fig. 10. According to this Fig. 10, the power stage interacts with the control block (proposed adaptive controller, Kalman filters, and MPPT algorithm) via a serial connection. At each step, the simulator runs the power stage for one sample interval and exports the system output to the embedded F28M3x concerto system. When the embedded system receives signals from the simulator, it executes the code of the control block for one sample interval. Then, the embedded system returns its control signals computed to the simulator via the same serial connection during this time interval. At this point, one sample cycle of the simulation is complete, and the simulator proceeds to the following sample interval. The PIL simulation approach is a powerful tool because easily allows executing the control block of a specific application on an embedded system or microcontroller in order to validate and demonstrate its performance without an expensive experimental prototype representing the power stages depicted in Fig. 10.

The detailed connection diagram of the control block depicted in Fig. 10 is shown in Fig. 11. According to this Fig. 11, first, the MPPT algorithm computes a new value of the optimal current trajectory, $i_{dc,opt}$, based on the filtered values

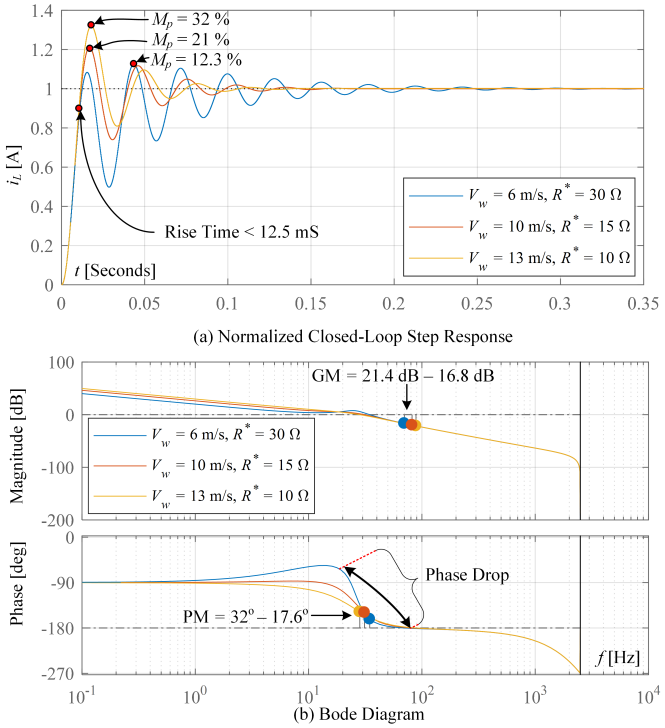

Fig. 9. Normalized closed-loop step response and the Bode diagram of the discrete system (11) via the tuned PI controller versus different V_w values.

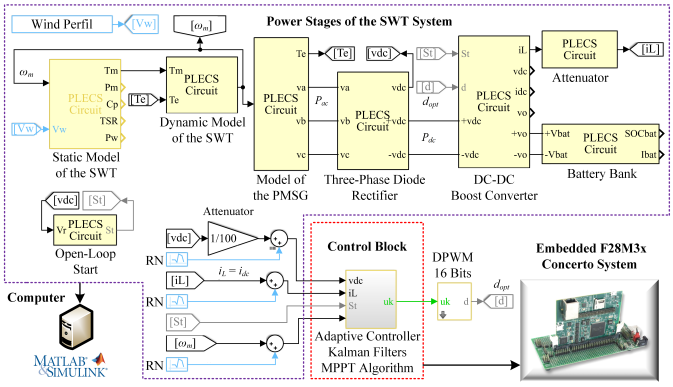

Fig. 10. Block diagram of the small-scale wind turbine system circuit implementation based on the PIL simulation approach.

of the rotational speed, ω_m, every 10 ms. Then, the proposed adaptive controller is computed in 2.0 e^{-4} s based on the values of the variable operation point, R^*, and the optimal current trajectory, $i_{dc,opt}$, and the electrical measurements of the inductor current, i_L, and the rectifier output voltage, v_{dc}, to ensure an appropriate optimal duty cycle signal, d_{opt}. The rate transition blocks (RT) handle data transfer between simulation blocks operating at different rates. The double-blocks convert the real-world input data to a double data type, and the $Div/0$ blocks avoid undefined results during the control block execution.

B. Simulation Results

Performing a wind profile with different step values of wind speed, V_w, in the small-scale wind turbine system, Figs. 12 (a) and (b) show the performance of both the proposed adaptive controller and tuned PI controller along the tracking process of

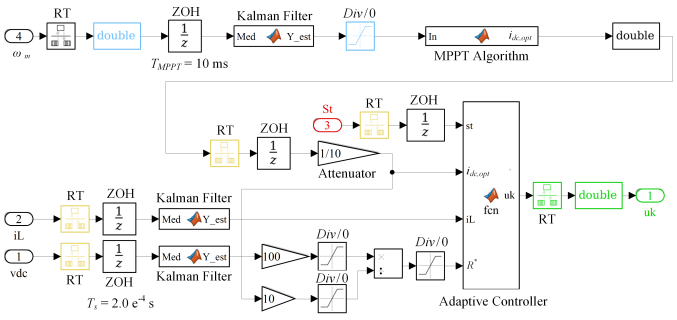

Fig. 11. Detailed connection diagram of the control block.

the optimal current trajectory, $i_{dc,opt}$, with and without the RN conditions, Kalman filters, and SWT dynamics, respectively. The parameters obtained with the proposed adaptive controller for the different wind speeds depicted in Fig. 12 (b) and other wind speeds, are shown in Table III of the appendix.

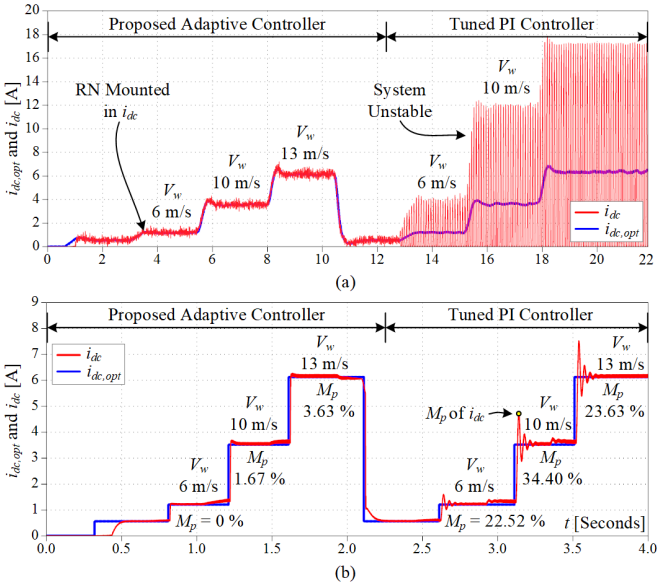

Fig. 12. The $i_{dc,opt}$ tracking process performance achieved via the proposed adaptive controller and the tuned PI controller; (a) with and (b) without the RN conditions, Kalman filters, and SWT dynamics.

Figs. 13 (a) and (b) show the tracking process performance of the optimal current trajectory, $i_{dc,opt}$, and the SWT's aerodynamic efficiency achieved with the proposed adaptive controller, respectively. The above, using a severe wind profile as depicted in Fig. 13 (c), which consists of a region of steps and a second region of fluctuations with low- and high-frequency power components.

Considering the wind profile of Fig. 13 (c), RN conditions, Kalman filters, and SWT dynamics, Fig. 14 shows the mechanical power achieved using the proposed adaptive controller, $P_{m,PAC}$, and the tuned PI controller,$P_{m,TPIC}$, versus its optimal, $P_{m,opt}$, value.

The rotational speed, ω_m, versus mechanical power curves at various wind speeds, V_w, as well as the simulated, $P_{m,opt,sim}$, and experimental, $P_{m,opt,exp}$, optimal mechanical power trajectory are shown in Fig. 15. The simulated trajectory was obtained with the proposed adaptive controller. The power curves and the experimental trajectory were obtained from the data set of the FESTO wind turbine learning system in the

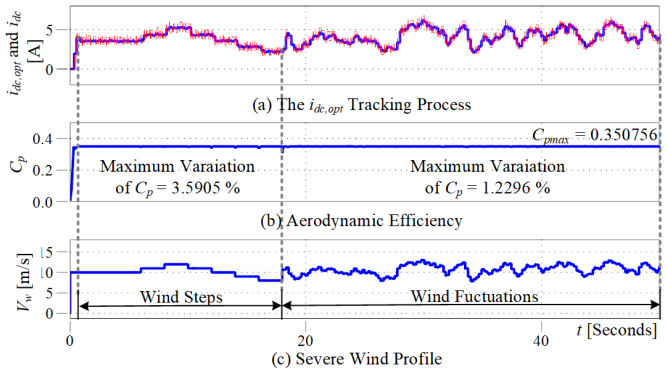

Fig. 13. The $i_{dc,opt}$ tracking process performance and the SWT's aerodynamic efficiency achieved via the proposed adaptive controller using the severe wind profile.

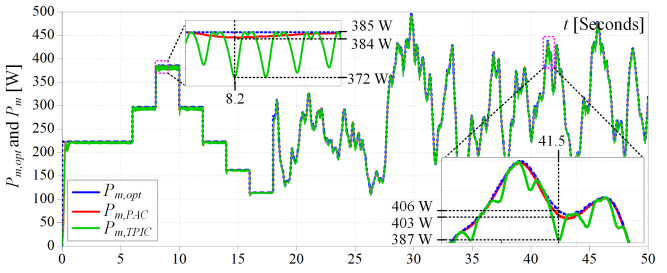

Fig. 14. The mechanical power achieved via the the proposed adaptive controller and the tuned PI controller vs. its optimal value.

previous work [30]. The optimal mechanical power trajectory in Fig. 15 connects the MPPs at different wind speeds.

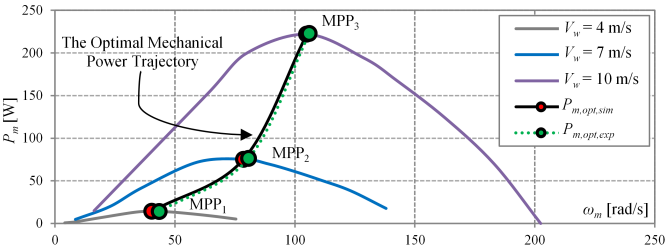

Fig. 15. The experimental and simulated mechanical power of the SWT as function of the rotational speed for different wind speeds.

Based on Fig. 15, the rotational speed, ω_m, versus turbine torque characteristics can be extracted, as shown in Fig. 16. This figure shows that the simulated, $T_{m,opt,exp}$, and experimental, $T_{m,opt,exp}$, optimal torque trajectory do not match the maximum torque point of each torque curve.

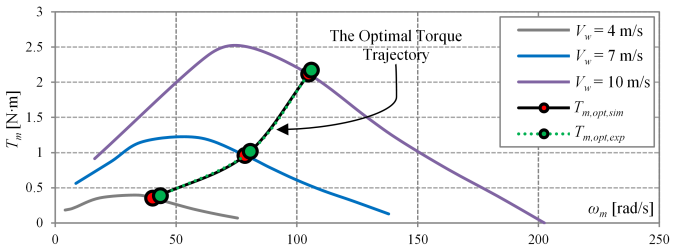

Fig. 16. The experimental and simulated torque of the SWT as function of the rotational speed for different wind speeds.

The experimental, $C_{p,exp}$, and simulated, $C_{p,sim}$, typical power coefficient curves of the SWT are depicted in Fig. 17. As in Fig. 16, the experimental and simulated curves were obtained from the data set of the FESTO wind turbine learning system and using the proposed adaptive controller, respectively.

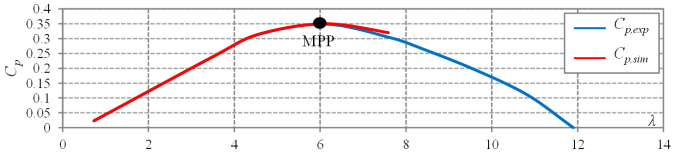

Fig. 17. Experimental and simulated typical power coefficient curves of the SWT as function of the λ vaue

.

C. Discussions

Considering wind steps, V_w, in the small-scale wind turbine system, Fig. 12 (b) shows that the proposed adaptive controller tracks the optimal current trajectory, $i_{dc,opt}$, with a minimum of oscillations and overshoots, M_p, below 4%; while the tuned PI controller leads to severe oscillations and overshoots, M_p, greater than 22%. Additionally, it can be deduced that the results of Fig. 12 (b) are approximate to those obtained in Fig. 8 (a) and Fig. 9 (b) via the current control scheme depicted in Fig. 7. This deduction supports that the approach used to design the adaptive mechanism algorithm of the controller is appropriate. Fig. 12 (a) shows that when the small-scale wind turbine system is evaluated against the wind steps, and external conditions are considered such as the dynamics of the Kalman filters and the SWT, the tuned PI controller leads to unstability in the tracking process of the optimal current trajectory, $i_{dc,opt}$. In contrast, the proposed adaptive controller maintains a better tracking process of the optimal current trajectory, $i_{dc,opt}$, without large oscillations and overshoots, M_p, as shown in Fig. 12 (a). The unstability depicted in Fig. 12 (a) is because the PI controller causes a severe phase drop (see Fig. 9), leading to high sensitivity in the changes of the overshoots, M_p, and oscillations in the inductor current, i_L, versus different values of wind speed, V_w, and external situations.

It can be seen in Fig. 13 (a) that the proposed adaptive controller maintains the tracking process of the optimal current trajectory, $i_{dc,opt}$, without large oscillations and overshoots, M_p versus the severe wind profile. This tracking process allows the aerodynamic efficiency of the SWT to be kept close to its maximum value ($C_{pmax} = 0.350756$) for the entire severe wind profile, as shown in Fig. 13 (b). Besides, the value of the power coefficient, C_p, of the SWT is maintained with a 3.5905% maximum variation concerning its maximum value for the region of wind steps; meanwhile, for the wind fluctuation region, the maximum variation is 1.2296%. The simulation results depicted in Fig. 14 showed that at $t = 8.2$ s and $t = 41.5$ s, the proposed adaptive controller maintained a maximum mechanical power variation of 1 W and 3 W versus its optimal value, respectively. In contrast, the tuned PI controller maintained a maximum mechanical power variation

of 13 W at $t = 8.2$ s and 19 W at $t = 41.5$ s versus its optimal value, with large mechanical power oscillations due to unstability conditions depicted in Fig. 12 (a). These results demonstrate that compared to the tuned PI controller, the proposed adaptive controller extracts higher mechanical power of the SWT, which positively impacts its MPPT process efficiency and MPP control. Based on the optimal current trajectory, $i_{dc,opt}$, the aerodynamic efficiency, C_p, and the mechanical power, P_m, achieved with the proposed adaptive controller, Figs. 15, 16, and 17, show that the optimal trajectories and the typical power coefficient curves obtained from simulation results are roughly similar to the experimental results obtained from the the data set of the FESTO wind turbine learning system.

According to the previous findings, the proposed adaptive controller can effectively track the optimal current trajectory, $i_{dc,opt}$, using two electrical measurements without large overshoots, M_p, and oscillations, leading to a stable SWT's aerodynamic efficiency along the MPPT process while effectively controlling the MPP of the small wind turbine. Additionally, the approach used in the adaptive mechanism algorithm leads to a low-cost and practical implementation of the controller in small-scale wind turbine systems as well as a practical implementation in low-end microcontrollers.

IV. Conclusions

An adaptive controller, whose adaptive mechanism algorithm is designed via the integration of the variable operation point of the small wind turbine into the discrete-time model of the dc-dc boost converter and the Bode stability criteria, was proposed in this paper. The adaptive controller processes the optimal current trajectory, $i_{dc,opt}$, estimated via the MPPT algorithm, to effectively attain the maximum aerodynamic efficiency and maximum power point of the SWT along the MPPT process. Furthermore, the approach used in the adaptive mechanism algorithm clearly indicates that the adaptive controller can operate with low estimation computational complexity in low-end microcontrollers without reference models and extra sensors; this form of operation results in a low-cost and practical implementation of the proposed controller in small-scale wind turbine systems.

The feasibility of our proposal was validated using the embedded system F28M35x and the PIL simulation approach considering RN conditions and the severe wind profile to achieve a more realistic simulation in the small-scale wind turbine system. The PIL simulation results clearly show that the proposed adaptive controller tracked the optimal current trajectory, $i_{dc,opt}$, with minimal oscillations in the inductor current, i_L, and an overshoot, M_p, at least 5.5 times lower than the tuned PI controller. Based on these results, the tracking process of the optimal current trajectory, $i_{dc,opt}$, was suitably performed via the proposed adaptive controller, leading to an aerodynamic efficiency close to its maximum value ($C_{pmax} = 0.350756$) and the maximum power point of the SWT along the MPPT process versus a severe wind profile. Additionally, the mechanical power variations against its optimum values, obtained with the proposed adaptive controller, remained at 1 W and 3 W at $t = 8.2$ s and $t = 41.5$ s, respectively, which were lower than those obtained with the tuned PI controller. These results positively impact the efficiency of the MPPT process and the control of the maximum power point of the SWT and achieve suitable simulated optimal trajectories of mechanical power and torque in the SWT, which were roughly similar to the experimental trajectories. The approach used in the controller adaptive mechanism algorithm can be applied in small-scale wind turbine systems operating with other types of dc-dc converters or extended to a cascade control scheme. This application or extension would inherit the same contributions claimed in this paper.

Appendix

TABLE I
PARAMETERS OF THE SWT MODEL.

Symbol	Parameter	Value
J	Inertia moment	0.0055 Kg·m^2
ρ	Air density	1.225 Kg/m^3
R_r	Radius	0.575 m
c_1, c_2, c_3		$5.837e^{-7}$, $2.823e^{-5}$, 0.000509
c_4, c_5, c_6	C_p constants	-0.004067, 0.01159, 0.005924
c_7, and c_8		0.01586, 0.005284

TABLE II
PARAMETERS OF THE PMSG GENERATOR.

Symbol	Parameter	Value
R_s	Phase resistance	2.6 Ω
L_q, L_d	d-q inductances	1.6 mH
Ψ_m	Magnetic flux	0.0592 v·s/rad
p	No. of poles	6

TABLE III
PARAMETERS OF THE PROPOSED ADAPTIVE CONTROLLER.

V_w [m/s]	b_1	b_2	b_3	a_2	a_3
4	$2.757e^6$	$-5.488e^5$	$2.732e^5$	-1.992	0.9918
5	$2.757e^6$	$-5.480e^5$	$2.723e^5$	-1.989	0.9888
6	$2.757e^6$	$-5.476e^5$	$2.719e^5$	-1.987	0.9872
7	$2.757e^6$	$-5.465e^5$	$2.708e^5$	-1.983	0.9832
8	$2.757e^6$	$-5.456e^5$	$2.699e^5$	-1.980	0.9800
9	$2.757e^6$	$-5.446e^5$	$2.689e^5$	-1.976	0.9764
10	$2.757e^6$	$-5.434e^5$	$2.678e^5$	-1.972	0.9721
11	$2.757e^6$	$-5.423e^5$	$2.667e^5$	-1.968	0.9681
12	$2.757e^6$	$-5.409e^5$	$2.653e^5$	-1.963	0.9631
13	$2.757e^6$	$-5.398e^5$	$2.642e^5$	-1.959	0.9588

Acknowledgment

Authors would like to thank Tecnológico Nacional de México (TecNM) for the financial support given to this research project under grant number: 5343.19-P.

References

[1] J. Plaza Castillo, C. Daza Mafiolis, E. Coral Escobar, A. Garcia Barrientos, and R. Villafuerte Segura, "Design, construction and implementation of a low cost solar-wind hybrid energy system," *IEEE Latin America Transactions*, vol. 13, no. 10, pp. 3304–3309, 2015.

[2] S. Bagawade, S. Eren, P. Jain, and M. Pahlevani, "Adaptive proportional-resonant controller based reactive power control for wind energy conversion systems," in *2017 IEEE Applied Power Electronics Conference and Exposition (APEC)*, pp. 1369–1374, 2017.

[3] E. Koutroulis and K. Kalaitzakis, "Design of a maximum power tracking system for wind-energy-conversion applications," *IEEE Transactions on Industrial Electronics*, vol. 53, no. 2, pp. 486–494, 2006.

[4] M. M. R. Singaravel and S. A. Daniel, "MPPT with single DC–DC converter and inverter for grid-connected hybrid wind-driven PMSG–PV system," *IEEE Transactions on Industrial Electronics*, vol. 62, no. 8, pp. 4849–4857, 2015.

[5] H. Fathabadi, "Novel maximum electrical and mechanical power tracking controllers for wind energy conversion systems," *IEEE Journal of Emerging and Selected Topics in Power Electronics*, vol. 5, no. 4, pp. 1739–1745, 2017.

[6] A. Urtasun, P. Sanchis, and L. Marroyo, "Small wind turbine sensorless MPPT: Robustness analysis and lossless approach," *IEEE Transactions on Industry Applications*, vol. 50, no. 6, pp. 4113–4121, 2014.

[7] C.-Y. Lee, P.-H. Chen, and Y.-X. Shen, "Maximum power point tracking (MPPT) system of small wind power generator using RBFNN approach," vol. 38, no. 10, 2011.

[8] Z. M. Dalala, Z. U. Zahid, W. Yu, Y. Cho, and J.-S. Lai, "Design and analysis of an MPPT technique for small-scale wind energy conversion systems," *IEEE Transactions on Energy Conversion*, vol. 28, no. 3, pp. 756–767, 2013.

[9] D. Zammit, C. Spiteri Staines, A. Micallef, and M. Apap, "MPPT with current control for a PMSG small wind turbine in a grid-connected DC microgrid," in *Wind Energy Exploitation in Urban Environment* (L. Battisti and M. Ricci, eds.), (Cham), pp. 205–219, Springer International Publishing, 2018.

[10] Y. Xia, K. H. Ahmed, and B. W. Williams, "A new maximum power point tracking technique for permanent magnet synchronous generator based wind energy conversion system," *IEEE Transactions on Power Electronics*, vol. 26, no. 12, pp. 3609–3620, 2011.

[11] N. Mendis, K. M. Muttaqi, S. Sayeef, and S. Perera, "Standalone operation of wind turbine-based variable speed generators with maximum power extraction capability," *IEEE Transactions on Energy Conversion*, vol. 27, no. 4, pp. 822–834, 2012.

[12] N. Mendis, K. M. Muttaqi, and S. Perera, "Management of battery-supercapacitor hybrid energy storage and synchronous condenser for isolated operation of PMSG based variable-speed wind turbine generating systems," *IEEE Transactions on Smart Grid*, vol. 5, no. 2, pp. 944–953, 2014.

[13] Y. Chen, G. Xiong, W. Li, J. Qian, and B. Hu, "The design of boost circuit in small wind generation system," in *Proceedings of 2013 IEEE International Conference on Service Operations and Logistics, and Informatics*, pp. 354–359, 2013.

[14] N. Mohan, T. M. Undeland, and W. P. Robbins, *Power Electronics. Converters, Applications and Design*. John Wiley and Sons, Inc, third ed., 2003.

[15] K. Ogata, *Sistemas de control en tiempo discreto*. Pearson Educación, 1996.

[16] T. Nuchkrua and T. Leephakpreeda, "Adaptive PID control of DC-link voltage via DC/DC buck-boost converter," *Science and Technology Asia*, vol. 18, no. 2, pp. 42–53, 2013.

[17] A. Aicha, M. Youcef, H. Said, and A. Tayeb, "Intelligent maximum power tracking control of PMSG wind energy conversion system," in *2017 5th International Conference on Electrical Engineering - Boumerdes (ICEE-B)*, pp. 1–6, 2017.

[18] L. V. Bellinaso, H. H. Figueira, M. F. Basquera, R. P. Vieira, H. A. Gründling, and L. Michels, "Cascade control with adaptive voltage controller applied to photovoltaic boost converters," *IEEE Transactions on Industry Applications*, vol. 55, no. 2, pp. 1903–1912, 2019.

[19] R. K. Subroto, L. Ardhenta, and E. Maulana, "A novel of adaptive sliding mode controller with observer for DC/DC boost converters in photovoltaic system," in *2017 5th International Conference on Electrical, Electronics and Information Engineering (ICEEIE)*, pp. 9–14, 2017.

[20] L. Ardhenta, R. K. Subroto, and P. Kuswiradyo, "Adaptive control for buck converter in hybrid power system based on DMRAC method," in *2018 Electrical Power, Electronics, Communications, Controls and Informatics Seminar (EECCIS)*, pp. 282–286, 2018.

[21] C.-Y. Huang, C.-Y. Lai, and K.-T. Cheng, *Fundamentals of Algorithms*, pp. 173–234. 12 2009.

[22] S. A. Papathanassiou, *Models for variable speed wind turbines*. PhD thesis, National Technical University of Athens, 1997.

[23] W. Ahmed, "Mechanical modeling of wind turbine comparative study," *International Journal of Renewable Energy Research (IJRER)*, vol. 3, p. 94, 01 2013.

[24] Festo Didactic, "Small-scale wind power electricity generation training system." Accessed Oct. 9, 2021 [Online].

[25] H. Matayoshi, A. M. Howlader, M. Datta, and T. Senjyu, "Control strategy of pmsg based wind energy conversion system under strong wind conditions," *Energy for Sustainable Development*, vol. 45, pp. 211–218, 2018.

[26] N. K. Umpol Seedadee, Sarayooth Vaivudh and P. Maneechot, "Power control system of small scale wind turbine using PSF technique," *Journal of Renewable Energy and Smart Grid Technology*, vol. 10, pp. 67–74, 09 2015.

[27] M. Chen and G. Rincon-Mora, "Accurate electrical battery model capable of predicting runtime and i-v performance," *IEEE Transactions on Energy Conversion*, vol. 21, no. 2, pp. 504–511, 2006.

[28] Q. Li, R. Li, K. Ji, and W. Dai, "Kalman filter and its application," in *2015 8th International Conference on Intelligent Networks and Intelligent Systems (ICINIS)*, pp. 74–77, 2015.

[29] A. M. Eltamaly and H. M. Farh, "Maximum power extraction from wind energy system based on fuzzy logic control," *Electric Power Systems Research*, vol. 97, pp. 144–150, 2013.

[30] D. R. Lopez-Flores, J. L. Durán-Gómez, and J. Vega-Pineda, "Aerodynamic frequency domain model for evaluating small wind turbines," in *2020 IEEE Applied Power Electronics Conference and Exposition (APEC)*, pp. 3276–3281, 2020.

[31] R. Sharma and S. Suhag, "Novel control strategy for hybrid renewable energy-based standalone system," *Turkish J. Electr. Eng. Comput. Sci.*, vol. 25, pp. 2261–2277, 2017.

[32] A. M. R. Amaral and A. J. M. Cardoso, "An economic offline technique for estimating the equivalent circuit of aluminum electrolytic capacitors," *IEEE Transactions on Instrumentation and Measurement*, vol. 57, no. 12, pp. 2697–2710, 2008.

[33] D. R. Lopez-Flores, J. L. Duran-Gomez, and M. I. Chacon-Murguia, "A mechanical sensorless mppt algorithm for a wind energy conversion system based on a modular multilayer perceptron and a processor-in-the-loop approach," *Electr. Power Syst. Res.*, vol. 186, p. 106409, 2020.

David R. López-Flores obtained the degree of Electronic Engineering, 2002 from the Instituto Tecnológico de Los Mochis, Sin., México, and the degree of Master of Science in Electronic Engineering, 2005, from the Instituto Tecnológico de Chihuahua Chih., México. Currently, he is a doctoral student at the Tecnológico Nacional de México / IT de Chihuahua. He is interested in power electronic systems for the conditioning of renewable energies.

José L. Durán-Gómez (M'96–SM'06) received the B.E. degree in industrial engineering in electronics and the M.Sc. degree in electronic engineering from Chihuahua Institute of Technology, Chihuahua, México, in 1988 and 1990, respectively, and the Ph.D. degree in electrical engineering from Texas A&M University, College Station, TX, USA, in 2000. From February 2001 to July 2002, he was with the Micropower Group, Tyco Electronics Power Systems, Mesquite, TX, USA, as a Member of Technical Staff. His research interests are primarily in power electronic converters and their control, power conditioning of renewable resources and power quality issues. He is the Lead Developer of the Power Electronics and Power Quality Laboratory at Chihuahua Institute of Technology, and is actively involved in academic projects while engaged in teaching and research activities.

Javier Vega-Pineda received the B.S. degree in Industrial Electronics Engineering from Instituto Tecnológico de Chihuahua (ITCH), México, the M.Sc. degree in Electronics from Instituto Nacional de Astrofísica, Óptica y Electrónica (INAOE), Tonantzintla, Puebla, México, and the Ph.D. in Computer Engineering from The University of Texas at El Paso (UTEP), Texas, USA, in 1977, 1980 and 1997, respectively. He was software engineer at National Cash Register (NCR) Industrial de México in 1980, and since 1981, he has been with the ITCH as Professor in the Electrical Engineering Department. From March 2004 to May 2006, he was Chairman of the ITCH Graduate School. His interest has been in the area of digital signal processing (DSP).